Anomalous Nernst and Seebeck coefficients in epitaxial thin film math xmlns="http://www.w3.org/1998/Math/MathML">mrow>msub>mi>Co/mi>mn>2/mn>/msub>msub>mi>MnAl/mi>mi>x/mi>/msub>msub>mi>Si/mi>mrow>mn>1/mn>mo>−/mo>mi>x/mi>/mrow>/msub>/mrow>/math> and math xmlns="http://www.w3.org/1998/Math/MathML">mrow>msub>mi>Co/mi>mn>2/mn>/msub>mi>FeAl/mi>/mrow>/math>

A. T. Breidenbach, H. Yu, T. A. Peterson, A. P. McFadden, W. K. Peria, C. J. Palmstrøm, and P. A. Crowell

Phys. Rev. B **105**, 144405 — Published 6 April 2022

DOI: 10.1103/PhysRevB.105.144405

2212-

2215/

Anomalous Nernst and Seebeck coefficients in epitaxial thin film $Co_2MnAl_xSi_{1-x}$ and Co_2FeAl

A. T. Breidenbach,[1] H. Yu,[1] T. A. Peterson,[1] A. P. McFadden,[2]
W. K. Peria,[1] C. J. Palmstrøm[2,3] and P. A. Crowell[1]
[1]*School of Physics and Astronomy,*
University of Minnesota, Minneapolis, Minnesota 55455
[2]*Department of Electrical & Computer Engineering,*
University of California, Santa Barbara, California 93106
[3]*Department of Materials, University of California, Santa Barbara, California 93106*

(Dated: March 21, 2022)

Abstract

We have measured the Seebeck and anomalous Nernst coefficients and corresponding transverse and longitudinal thermoelectric conductivities from 2 to 400 K in thin film (thickness $t \sim 10$ nm) $Co_2MnAl_xSi_{1-x}$ ($0 \leq x \leq 1$) and Co_2FeAl grown by molecular beam epitaxy (MBE). A large (-14 A·m^{-1}K^{-1} at 300 K) anomalous component of the transverse thermoelectric conductivity is observed in Co_2MnAl, especially as contrasted to Co_2MnSi (0.28 A·m^{-1}K^{-1} at 300 K). This enhancement is likely due to Weyl points close to the Fermi level of Co_2MnAl which disappear as x decreases.

I. INTRODUCTION

Full Heusler alloys of the form X_2YZ, where X and Y are transition metals and Z is a p-block element, are a large and diverse family of compounds, including metals, semiconductors, ferromagnets and antiferromagnets [1]. In particular, Co_2MnSi has been predicted [2, 3] and confirmed [4] to be completely half-metallic, as suggested by photoemission measurements [5]. This high degree of spin polarization typically leads to large tunneling magnetoresistance (TMR), which makes such Heuslers of particular interest in spintronic applications such as spin valves [6, 7]. High spin polarization also leads to low Gilbert damping, which allows for higher switching frequency spin transfer torque applications [8, 9]. Motivated by such applications, there has been considerable theoretical effort dedicated to determining the density of states (DOS) of cobalt-based full Heuslers and its impact on electronic properties. On the other hand, the bulk of experimental efforts focus on electrical transport properties, which rely on interpretation in order to extract quantities such as the spin polarization at the Fermi level. Some of the more common approaches, such as anomalous Hall effect (AHE) measurements [10], are in fact the least suitable for probing the spin polarization. In principle, if an intrinsic AHE mechanism dominates, the AHE should be directly proportional to the spin polarization of the density of states at the Fermi level [11]. It is well known, however, that in many materials extrinsic contributions such as side-jump and skew scattering [12, 13] are significant and can contaminate the proportionality between the AHE and spin polarization. Therefore, considerable theoretical work must be done to compute Berry curvatures and show that intrinsic mechanisms dominate for a given material [11], therefore justifying the use of the AHE to infer spin polarization. In the worst case,

extrinsic mechanisms may contribute enough so that no definitive quantitative conclusions can be drawn.

The magneto-thermoelectric effects (MTEs) provide complementary information to electrical transport coefficients as they can be related to derivatives of conductivity through the Mott relations. Furthermore, the dependence of the magneto-thermoelectric coeffecients on energy derivatives of the conductivity also makes them particularly sensitive probes of intrinsic mechanisms resulting from anomalies in band structures near the Fermi level [14]. A final noteworthy motivator for the measurement of MTEs in Heusler compounds is that they are strong candidates for thermoelectric materials. Recently, proposed thermoelectric devices that utilize the anomalous Nernst effect (ANE) instead of the Seebeck effect have drawn experimental attention [15–17].

In this article, we report on the Seebeck and anomalous Nernst coefficients over a range from 2-400 K in the Heusler series $Co_2MnAl_xSi_{1-x}$ (x=0, 0.33, 0.67 and 1) as well as Co_2FeAl. These coefficients are obtained through the fabrication of thermoelectric measurement devices and a second harmonic ac detection scheme. We find that the relative magnitudes of the ANCs in the $Co_2MnAl_xSi_{1-x}$ series are in qualitative agreement with their theoretically computed spin-resolved band structures [3, 18, 19].

II. THEORETICAL BACKGROUND

Mott *et al.* [20] showed that in the relaxation time approximation to the Boltzmann equation, one can derive an expression for the thermoelectric tensor, which includes the Seebeck coefficient S_{xx} and Nernst coefficient S_{xy}, for a single band metal as

$$\mathbf{S} = \frac{k_B}{e\boldsymbol{\sigma}} \int \frac{E-\mu}{k_B T} \boldsymbol{\sigma}(E) \frac{df(E)}{dE} dE, \tag{1}$$

where $f(E)$ is the Fermi-Dirac distribution, μ is the chemical potential, and $\boldsymbol{\sigma}(E)$ is the energy-dependent conductivity tensor. Performing a Sommerfeld expansion of Eq. 1 at low temperatures then yields

$$\mathbf{S} = -\frac{\pi^2 k_b^2 T}{3e} \frac{1}{\boldsymbol{\sigma}} \frac{d\boldsymbol{\sigma}(\mu)}{dE} + O[T^3], \tag{2}$$

which is accurate to order $(\frac{k_b T}{E_f})^2$. These expansion relations are known collectively as Mott relations, which have proven widely applicable in relating electrical transport coefficients to thermoelectric coefficients. Critically, Eq. 2 establishes that thermoelectric coefficients are

proportional to the energy derivatives of DOS-related quantities such as $\boldsymbol{\sigma}(E)$, as opposed to the ordinary electrical transport coefficients, which follow direct proportionalities.

The ANC can be derived from a general charge current $\boldsymbol{J}$ under the influence of the electric field $\boldsymbol{E}$ in the presence of a temperature gradient ∇T:

$$\boldsymbol{J} = \sigma \cdot \boldsymbol{E} - \alpha \cdot \nabla T, \tag{3}$$

in which σ is the conductivity tensor and α is the Peltier tensor. We consider a thin film sample in the xy plane. Under open circuit conditions ($J = 0$) and with ∇T in the x direction, one can write out the transverse component E_y as:

$$E_y = \frac{\sigma_{xx}\alpha_{xy} - \sigma_{xy}\alpha_{xx}}{\sigma_{xx}^2 + \sigma_{xy}^2} \cdot \nabla T \ . \tag{4}$$

Since usually $\sigma_{xx}^2 \gg \sigma_{xy}^2$, the ANC S_{xy}^A defined as $E_y/\nabla T$ can now be expressed with $\rho_{xx} = 1/\sigma_{xx}$ and $\rho_{xy} = -\sigma_{xy}/\sigma_{xx}^2$ [15]:

$$S_{xy}^A = \rho_{xx}\alpha_{xy}^A + \rho_{xy}^A\alpha_{xx} \ , \tag{5}$$

where α_{xx} is the longitudinal thermoelectric conductivity (LTC), α_{xy}^A is the anomalous component of the transverse thermoelectric conductivity (TTC), and ρ_{xy}^A is the anomalous Hall resistivity. Equation 5 allows us to infer α_{xy}^A of a given material, as all other quantities in the equation can be directly measured. Because the thermoelectric coefficients can be described by the dependence of σ on electrochemical potential through the Mott relations, a Sommerfeld expansion, which is expected to hold for low temperatures, gives [14]:

$$\alpha_{xx} = -\frac{\pi^2 k_b^2 T}{3e}\frac{d\sigma_{xx}(\mu)}{dE} \ , \tag{6}$$

$$\alpha_{xy}^A = -\frac{\pi^2 k_b^2 T}{3e}\frac{d\sigma_{xy}^A(\mu)}{dE} \ . \tag{7}$$

From Eqs. 6 and 7, we are able to correlate α_{xx} and α_{xy}^A to energy derivatives of the conductivity. Nonetheless, the conductivity can be thought of in a Drude-like sense as the product of the energy-resolved DOS and a relaxation time. Thus, qualitative information about the DOS can be acquired from the Seebeck and ANE coefficients.

Although extrinsic effects such as skew scattering could also contribute to the AHC, here we focus on the intrinsic contribution. It can be shown that the intrinsic AHC can be

calculated with the Berry curvature, $\Omega_z(\mathbf{k})$, integrated over all filled bands [10, 11, 14, 21],

$$\sigma_{xy}^{A} = -\frac{e^2}{\hbar}\int \frac{d\mathbf{k}}{(2\pi)^3}\Omega_z(\mathbf{k})\Theta(E_F - \epsilon(\mathbf{k})) \ . \tag{8}$$

This makes the AHC a useful probe to search for topological features such as Weyl points (which act as sources and sinks of the Berry curvature) in the band structure. Applying Eq. 8 to Eq. 7 gives [15] :

$$\alpha_{xy}^{A} = -\frac{e^2}{\hbar}\int \frac{d\mathbf{k}}{(2\pi)^3}\Omega_z(\mathbf{k})\delta(E_F - \epsilon(\mathbf{k})) \ . \tag{9}$$

Unlike the AHC, in which the Berry curvature is integrated over all occupied bands, only bands near the Fermi level can contribute to α_{xy}^{A}. This makes α_{xy}^{A} extremely sensitive to the position of the Fermi level, and therefore capable of capturing the topological features, even if they are too weak to show influence in the AHE [22].

The above theory is widely applicable to most ferromagnets, especially at low temperatures. However, it is of note that in systems where the Fermi level lies near a maximum or minimum point in the DOS, the Mott relations of Eqs. 6 and 7 may break down to some extent [15]. Although the Mott relations are still obeyed at sufficiently low temperatures, expansion about Weyl points reveals the presence of an additional temperature scaling proportional to $T \ln T$ [15]. Such a scaling has already been observed in Co_2MnGa, which has its Fermi level near such Weyl points and is qualitatively similar to Co_2MnAl in band structure[3, 15, 23]. As such, one might expect to also see a strong $T \ln T$ dependence in the α_{xy}^{A} of Co_2MnAl. This $T \ln T$ dependence should be weaker in materials where Weyl points are not expected to be close to the Fermi level.

III. SAMPLES

The samples measured in this study are Co_2FeAl and the quaternary series $Co_2MnAl_xSi_{1-x}$ for $x = 0$, 0.33, 0.67, and 1. These Heusler compounds are grown as thin films (10 nm thickness on MgO(001) substrates) by molecular beam epitaxy (MBE). The samples were grown on a MgO buffer layer (prepared by e-beam evaporation at a substrate temperature of 630 °C) and subsequently annealed at 600 °C. In general this approach yields films with at least B2 ordering, with a significant fraction of the fully-ordered $L2_1$ phase when the composition is near $x = 0$ [24, 25]. Estimates of the phase composition were obtained by

X-ray diffraction (XRD) measurements. In-plane rotation scans (ϕ scans) for Co_2MnSi, which is predominantly $L2_1$, and Co_2MnAl, which has no detectable $L2_1$ order, are shown in Figs. 1(a) and (b). The fourfold symmetry of the peaks indicates the samples are epitaxial. Following the approach of Webster[26] and Takamura[27], the $L2_1$ order parameter was determined by comparing the experimental intensity ratio of the (111) and (202) Bragg peaks with the theoretical ratio, while the B2 order parameter was determined by comparing the experimental intensity ratio of the (002) and (202) peaks with the theoretical value. The difference of the two order parameters gives the fraction of the sample that is B2 but not $L2_1$. The two order parameters are shown in Fig. 1(c) along with the B2 fraction determined from their difference. From the figure, it is clear that the samples are at least B2 ordered, with the notable exception of the $Co_2MnAl_{0.33}Si_{0.67}$ sample which has more disorder. In addition to this, Co_2MnSi has an $L2_1$ ordering fraction of 80%, which decreases with increasing Al concentration across the CMAS series. This decrease of $L2_1$ ordering is expected, and has been observed across other CMAS series [29].

For the CMAS series, the main effect of changing the Al-Si ratio is to shift the Fermi level, while the DOS is expected to maintain approximately the same shape. Such shifts can be monitored by measurement of the sign of the anisotropic magnetoresistance (AMR) ratio [30]. Figure 2 shows the AMR ratio as a function of the angle between the magnetization and current. Co_2MnAl exhibits a positive AMR ratio, which is consistent with the Fermi level being positioned near the edge of a half-metallic gap (the gap in minority spin band). This is in agreement with calculations of the DOS and other experimental measurements [3, 19]. With increasing Si concentration, the AMR reverses sign and grows in magnitude, with Co_2MnSi having a large negative AMR ratio. This is consistent with the hypothesis that the Fermi level of Co_2MnSi sits in the half-metallic gap, which is also confirmed by theoretical calculations of the DOS in addition to a giant measured TMR [3, 19, 31, 32].

The resistivity and the saturated anomalous Hall resistivity were measured as a function of temperature, as shown in Fig. 3. Additionally, the residual resistivity ratio (RRR), defined as $\rho(300\text{ K})/\rho(2\text{ K})$, was calculated for each sample and is given in Table I. (T= 10 K is used in the RRR for Co_2FeAl due to a lack of lower temperature resistivity data on this sample.) Note that Co_2MnSi in particular has a relatively high RRR of 2.5, which is likely related to its higher degree of $L2_1$ ordering.

In Fig. 4, a log-log plot of ρ_{xy}^A vs ρ_{xx} is shown, along with fits to the power law $\rho_{xy}^A = \sigma_{xy}^A \rho_{xx}^m$.

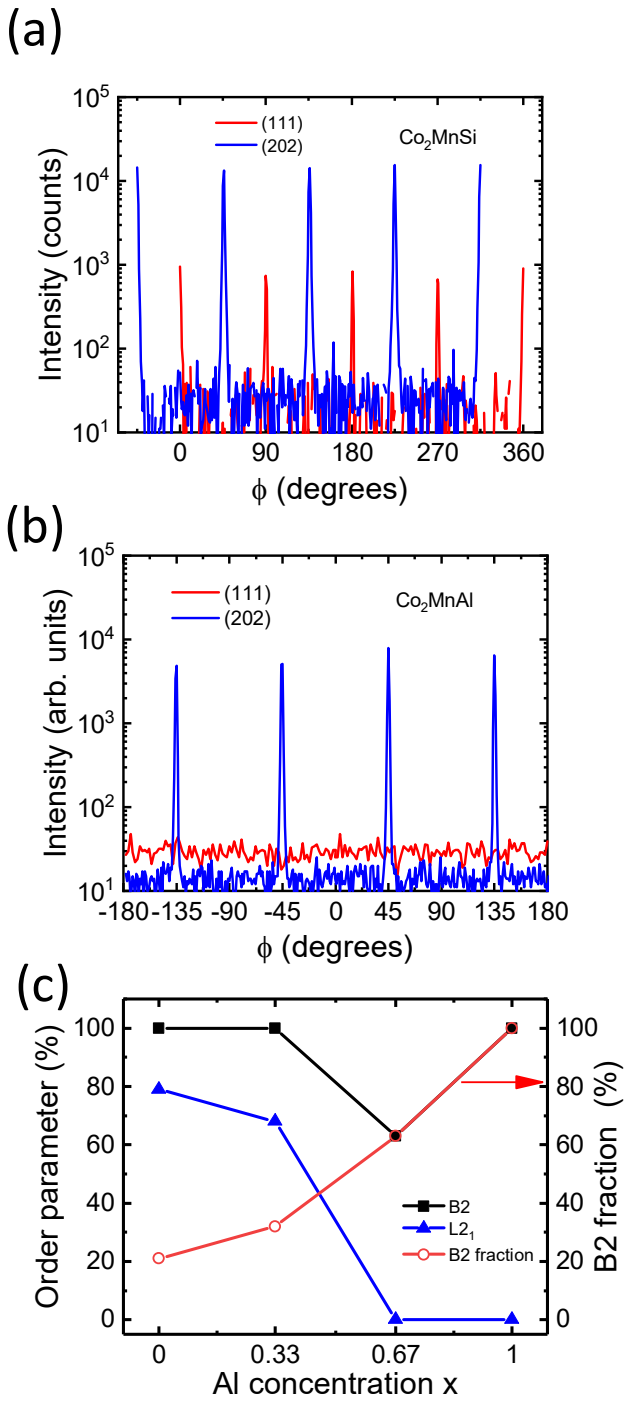

Figure 1: XRD wide angle scans and summary of lattice ordering. The fourfold symmetric (202) peaks in (a) Co_2MnAl and (b) Co_2MnSi (the latter published in our previous work [28]) indicate that the samples are epitaxial. Note the presence of the (111) peaks in the case of Co_2MnSi, indicating partial $L2_1$ ordering. (c) $L2_1$ and B2 order parameters as a function of the Al concentration in CMAS. The B2 order parameter (black squares) indicates the fraction of Co atoms on the appropriate sublattice. Subtracting the $L2_1$ order parameter yields the fraction of the sample that is only B2-ordered.

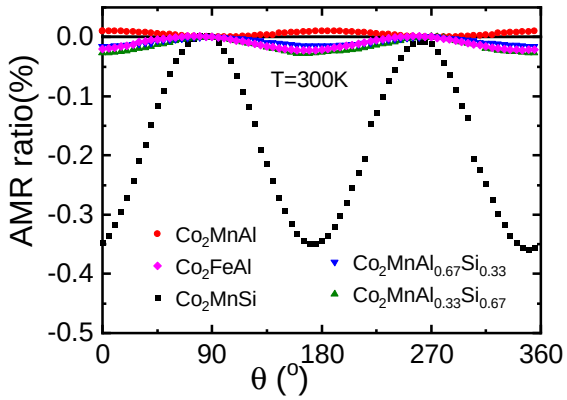

Figure 2: The AMR ratio for the Heusler thin film samples measured at 300 K as a function of angle between the magnetization and current. The AMR ratio is defined as AMR(θ)=($\rho(\theta)$-$\rho(90°)$)/$\rho(90°)$, with θ=0° corresponding to the angle at which the magnetization is parallel to the current.

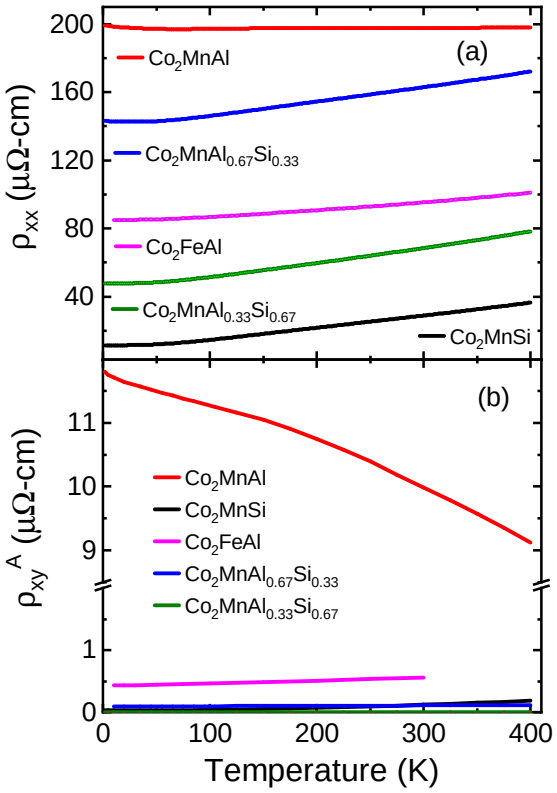

Figure 3: [Color Online] Summary of the temperature dependence of (a)resistivity and (b)anomalous Hall resistivity for the Heusler thin films.

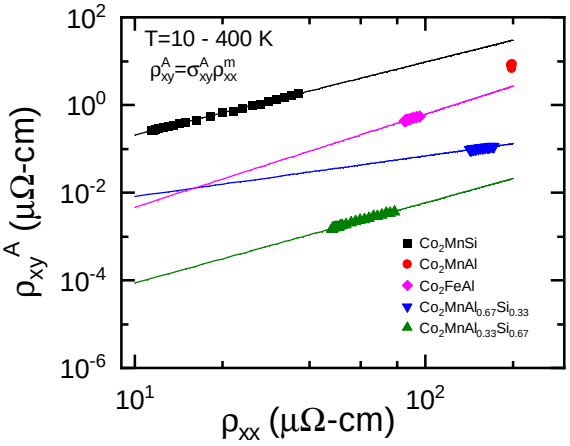

Figure 4: [Color Online] Summary plot of anomalous Hall resistivity vs longitudinal resistivity for Heusler alloy thin films, where temperature, which spans 2 to 400 K, is the implicit variable. The solid lines are fits to the power law $\rho_{xy}^A = \sigma_{xy}^A \rho_{xx}^m$. Fitted values of m are included in Table I. Note that no power-law fitting could be performed for Co_2MnAl since there was little change in the resistivity over the range 2 to 400 K.

This can be used to help determine whether the AHE is dominated by extrinsic contributions. If the skew scattering mechanism is dominant, the longitudinal resistivity, ρ_{xx}, should be directly proportional to the anomalous Hall resistivity ($m = 1$) [13]. Alternatively, $\rho_{xy}^A \propto \rho_{xx}^2$ implies that either side-jump scattering or an intrinsic mechanism dominates [12]. The fitted values of m and σ_{xy}^A are displayed in Table I. No sample shows perfect agreement with the $m = 2$ power law, implying that a significant skew scattering contribution is present in all samples except perhaps Co_2FeAl ($m = 2.12$). In particular, $Co_2MnAl_{0.67}Si_{0.33}$ has a slope of approximately 1 ($m = 0.92$), suggesting that skew scattering is likely to be dominant [13], which could be a result of the mixture of B2 and A2 ordering in this sample. It is important to note that in samples with slopes close to two, it is impossible to rule out the possibility of side-jump scattering with this method [12]. Therefore, using the AHE alone one cannot confirm that an intrinsic mechanism is significant in any of our Heusler samples. Furthermore, this analysis could not be performed for Co_2MnAl because ρ_{xx} depends only weakly on temperature over the range 2 to 400 K.

Ferromagnetic resonance (FMR) measurements have also been performed on all of these samples and reported in previous work [28], yielding their approximate saturation magne-

tizations (subject to small corrections due to interfacial anisotropy), which are shown in Table I. These measured values are in good agreement with the published values for these compounds [33, 34].

Table I: Summary sample characterization data of the thin film Heusler samples. The power law exponent is obtained from the fitting $\rho_{xy}^{A} = \sigma_{xy}^{A}\rho_{xx}^{m}$ of the data shown in Fig. 4

Sample	RRR	$4\pi M_s$ (emu/cm^3)	Power law exponent m
Co_2MnSi	2.5	1042	1.7
$Co_2MnAl_{0.33}Si_{0.67}$	1.4	1029	1.8
$Co_2MnAl_{0.67}Si_{0.33}$	1.1	1015	0.9
Co_2MnAl	1.0	930	N/A
Co_2FeAl	1.1	1234	2.1

IV. METHODS

The devices used to measure MTE coefficients of the CMAS samples were patterned with photolithography techniques, etched by ion milling, followed by deposition of Ti/Au contacts by e-beam evaporation. Critically, because we started with epitaxial thin films, all components of the thermoelectric device were patterned on the chip. A typical device used in these measurements is shown in Fig. 5(a), which is similar in design to the devices used in Refs. [35, 36]. The magnetic film under test is patterned into a Hall bar using Ar^+ ion milling to provide contact points for Seebeck and Nernst voltages. Subsequently a Ti(5 nm)/Au(50 nm) layer is deposited by e-beam evaporation at $\sim 10^{-6}$ Torr. The Ti/Au layer is patterned into bonding pads and vias, heaters, and a thermistor strip, all of which are electrically isolated by the insulating substrate.

The Au resistive heaters on either end of the Hall bar are used to create a temperature gradient $\partial_x T$ along the Hall bar where the condition $\partial_x T \gg \partial_y T$ is ensured by the device's aspect ratio. The thermistor strip can then be used to quantify the resultant temperature profile along the x-direction. Further information about thermometry calibration and usage is detailed in Appendix A. Because an ac excitation is used, the resulting temperature $T(x,t)$ is a function of position and time, and the phase and amplitude are a function of distance

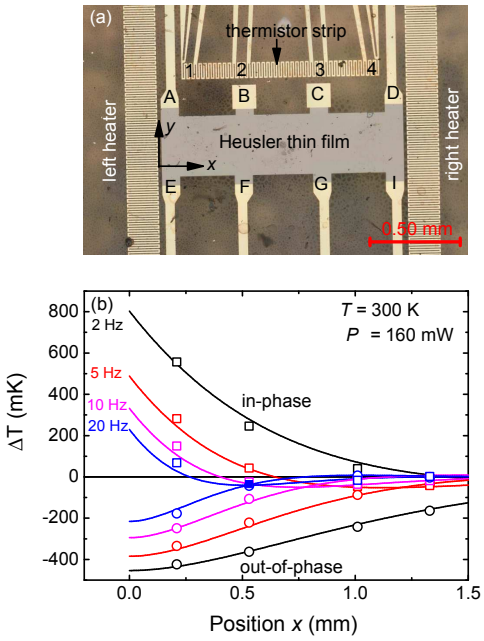

Figure 5: [Color Online] (a) Optical plan-view micrograph of the device design used to measure (magneto)-thermoelectric coefficients. All heaters, thermistors, and bonding pads are 5 nm Ti/50 nm Au. (b) Quadrature ΔT values for thermistors 1–4 as a function of coordinate x measured from the edge of the left heater. The squares are the in-phase with heater power component while the circles are the out-of-phase component, and data for several drive frequencies f are shown as indicated. The data shown in (b) are taken on a 12nm Co_2FeAl device on an MgO substrate at 9 mA RMS heater excitation, which corresponds to 160 mW.

x from the heaters. The measured temperature profile in Fig. 5(b) is fit according to the model

$$T(x,t) = A\frac{e^{-k|x|}}{2k}e^{i\omega' t}, k = i(\frac{r+i\omega'}{D})^{1/2}, \tag{10}$$

where k is the wave number of the temperature profile, D is the thermal diffusivity of the substrate, A is an overall scaling amplitude related to the heater power and chip/substrate heat capacities, and r is a phenomenological relaxation term representing heat leak through the substrate, which is thermally sunk to the copper block on which it is mounted. The derivation and assumptions behind this model are described in Appendix B. These fits can then be used in order to convert the measured Seebeck and Nernst voltages into coefficients. Details of the procedures used to calculate the Seebeck and anomalous Nernst coefficients

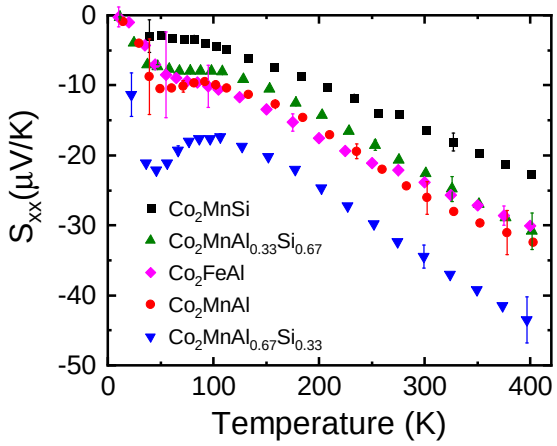

Figure 6: [Color Online] Temperature dependence of Seebeck coefficients for the Heusler thin films. The $Co_2MnAl_{0.67}Si_{0.33}$ sample has the largest magnitude of S_{xx}. The valleys at low temperatures are due to phonon drag, a well-documented effect in thermoelectrics.

are given in Appendices C and D.

V. THERMOELECTRIC COEFFICIENT RESULTS

A. Seebeck Coefficients in Heusler thin films

The Seebeck coefficient results as a function of temperature are summarized in Fig. 6, and $\alpha_{xx}(T)$ is shown in Fig. 7. The Seebeck coefficients for Co_2MnSi, Co_2MnAl, and Co_2FeAl at room temperature are slightly larger than the results on bulk Heusler samples reported by Hayashi *et al.* [37] and agree more closely with the values reported by Balke *et al.* [38]. Furthermore, the observed Seebeck coefficients in these thin-film Heusler alloys are large in comparison to other ferromagnetic metals. For comparison, the Seebeck coefficient is 15 μV/K in Fe and -19 μV/K in Ni at room temperature [39].

There are peaks or shoulders in the Seebeck coefficient at low temperature in all samples. These are due to phonon drag, a well-documented effect in thermoelectrics [40]. Phonon drag is only prevalent well below a material's Debye temperature, as it is suppressed by Umklapp phonon-phonon scattering at sufficiently high temperatures [39, 40]. Phonon-drag contributions are not captured by either of the Mott expressions (Eqs. 6 and 7) or the critical expansion of the α^A_{xy}, and so this contribution results in deviations from linear behavior in

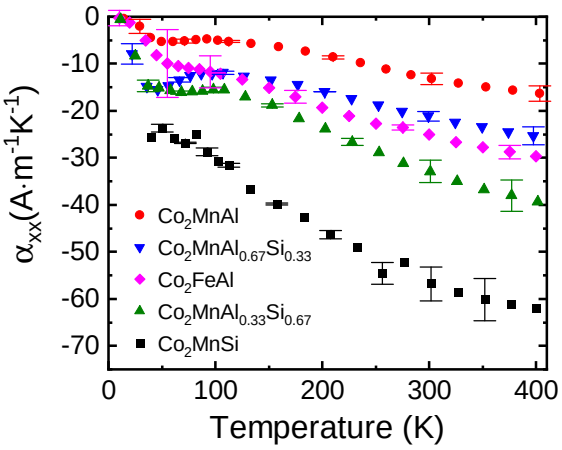

Figure 7: Longitudinal thermoelectric conductivity plotted as a function of temperature. Unlike S_{xx}, the magnitude of α_{xx} decreases with increasing Al composition.

both α_{xx} and α^A_{xy} at low temperatures.

The magnetic field dependence of S^A_{xy} at 300 K is shown in Fig. 8(a) for the different Al compositions, and the composition dependences of S_{xx} and S^A_{xy} are shown in Fig. 8(b). As Si is replaced by Al, the magnitude of S^A_{xy} gradually increases and the largest S^A_{xy} is observed for $Co_2MnAl_{0.67}Si_{0.33}$. Above Al-0.67, S^A_{xy} decreases but S^A_{xy} of Co_2MnAl remains larger than that of Co_2MnSi. Our Si composition dependences are in qualitative agreement with Ref. 41.

B. Anomalous Nernst coefficients in Heusler thin films

In Fig. 9, α^A_{xy} is plotted as a function of temperature from 2 to 400 K for the five different thin films. The magnitude of α^A_{xy} increases monotonically with Al concentration x. The Al-rich samples $Co_2MnAl_{0.67}Si_{0.33}$ and Co_2MnAl stand out due to their large values of α^A_{xy} at high T, which could be a result of the existence of Weyl points. Motivated by the linearization method proposed in [15], we consider the temperature dependence $\alpha^A_{xy}(T) = AT + BT\ln T$ above the phonon drag temperatures. A fit to this form is shown in Fig. 10, which shows $\alpha^A_{xy}(T)/T$ vs $\ln T$, and the corresponding fit parameters are provided in Table II. The parameter A increases in magnitude with increasing Al concentration, implying that $\frac{d\sigma^A_{xy}}{dE}$ increases as well, which is expected from the calculated CMAS band structures in Ref. 42. The coefficient B is positive and is larger in the Al-rich samples and nearly zero

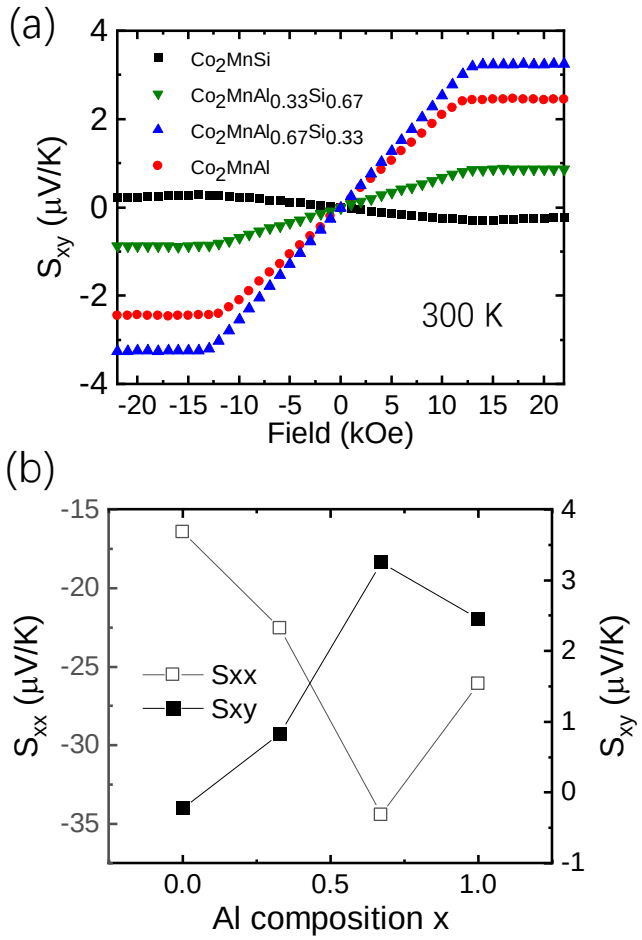

Figure 8: (a) S_{xy}^A at $T = 300$ K as a function of magnetic field for several different Al compositions. (b) Dependence of S_{xx} and S_{xy}^A at 300 K on the Al concentration.

for Co_2MnSi and $Co_2MnAl_{0.33}Si_{0.67}$. This is consistent with our expectations, given the apparent proximity of Weyl points near the Fermi level in Co_2MnAl. As noted by the authors of Ref. 15, this can cause the observed super-linear temperature dependence. We note, however, that given the limited range of $\ln T$ in Fig. 10, we are reluctant to assign much significance to the functional form assumed in the fit. The important point is the significant departure from linear behavior.

We have included literature values of α_{xy}^A (300 K) in Fig. 11 for comparison. From this

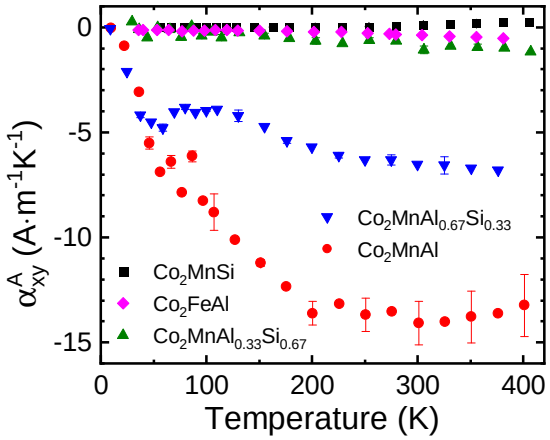

Figure 9: [Color Online] Summary of the temperature dependence of the anomalous component of the transverse thermoelectric conductivity for Heusler thin films. The magnitude of α^A_{xy} increases with increasing Al composition.

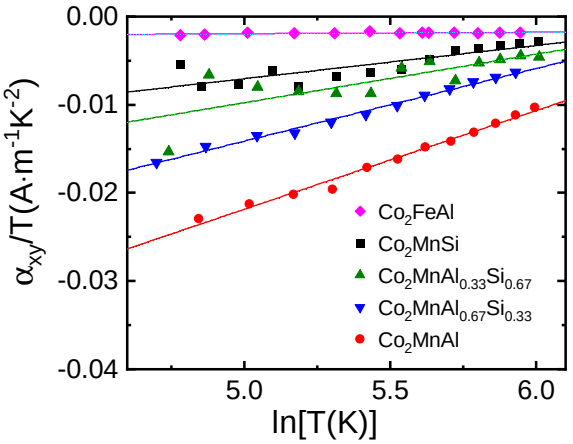

Figure 10: [Color Online] Fits of α^A_{xy} to the Weyl point expansion $\alpha^A_{xy}(T) = AT + BT\ln T$. Fits and data are plotted as $\alpha^A_{xy}(T)/T$ vs $\ln T$ to linearize the fit.

figure, it is apparent that α^A_{xy} is very large in Co_2MnAl. This further demonstrates that the existence of Weyl points could lead to a large α^A_{xy}, similar to Co_2MnGa [15]. Additionally, it is of note that the α^A_{xy} of Co_2MnSi is small compared with other ferromagnets, in spite of its large AHC and half metallicity. This is consistent with the absence of topological features in the band structure. Variations in the homogeneity and particularly the degree of $L2_1$ ordering are likely to impact the magnitudes to some degree, but we cannot hypothesize a

Table II: Extracted fitting parameters for fits to the model $\alpha_{xy}^{A}(T) = AT + BT\ln T$ for CMAS-x and CFA in addition to the inferred $d\sigma_{xy}^{A}/dE$

Sample	Co_2MnSi	$Co_2MnAl_{0.33}Si_{0.67}$	$Co_2MnAl_{0.67}Si_{0.33}$	Co_2MnAl	Co_2FeAl
A ($\mathrm{mA{\cdot}m^{-1}K^{-2}}$)	-2.6	-4.5	-100	-290	-0.038
B ($\mathrm{mA{\cdot}m^{-1}K^{-2}}$)	0.52	0.30	14	42	0.21
$\frac{d\sigma_{xy}^{A}}{dE}$ ($(\mu\Omega\ \mathrm{cm})^{-1}\mathrm{eV}^{-1}$)	1.1×10^{-3}	1.8×10^{-3}	0.042	0.12	1.6×10^{-5}

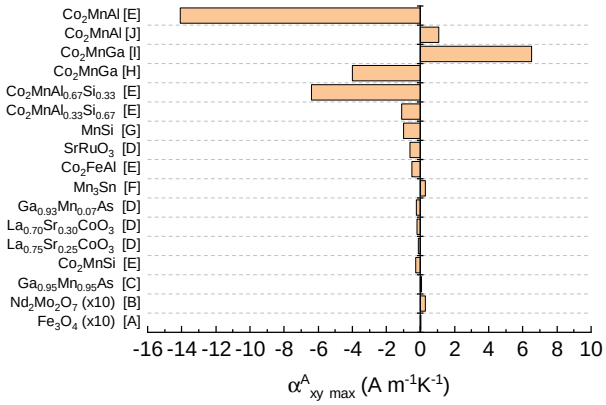

Figure 11: Comparison of literature values of α_{xy}^{A}. References correspond as follows: [A]=[43], [B]=[44], [C]= [45], [D]=[46], [E]=This work, [F]=[47, 48], [G]=[49], [H]=[15], [I]=[50], [J]=[41].

scenario in which disorder somehow increases the size of the ANC in Co_2MnAl, nor can it be responsible for the anomalous temperature dependence.

VI. DISCUSSION

The Mott relations in Eqs. 2 link the thermoelectric coefficients to the conductivity through its derivative with respect to energy, and the conductivity can be thought of in a Drude-like sense as the product of the energy-dependent DOS and a relaxation time. The measured large S_{xx} and α_{xx} with respect to common ferromagnets such as Fe and Ni therefore agree with expectations based on the DOS calculations in Ref. 42, in which $d\sigma_{xx}/dE$ at the Fermi level varies significantly with composition.

We observe a large ANC, α_{xy}^{A} in particular, in the Al-rich samples Co_2MnAl and $Co_2MnAl_{0.67}Si_{0.33}$, along with a large AHC in Co_2MnAl. Notably, Co_2MnAl, which shows the largest AHE, does not exhibit the largest ANE (S_{xy}^{A}). This is a result of the competition of the terms in Eq. 5: $\rho_{xx}\alpha_{xy}^{A}$ and $\rho_{xy}^{A}\alpha_{xx}$. Although each electronic resistivity ρ and thermoelectric conductivity α term are monotonic in x, the inverse x dependence of ρ and α makes their combinations nontrivial in x dependence. (For example, α_{xx} decreases with x but ρ_{xy}^{A} increases with x, therefore the $\rho_{xy}^{A}\alpha_{xx}$ becomes nonmonotonic.) This has also been discussed in Ref. 41. Unlike S_{xy}^{A}, the thermoelectric conductivities α_{xx} and α_{xy}^{A} show monotonic dependence as Al composition increases. This is because the thermoelectric conductivities are directly related to energy derivatives of the electronic conductivities, which is expected from Eqs. 6 and 7. We are not aware of Berry curvature calculations for $Co_2MnAl_{0.67}Si_{0.33}$, but Co_2MnAl is predicted to have Weyl points near the Fermi surface, which give rise to large σ_{xy}^{A} and α_{xy}^{A} [51]. The expected large AHE has been observed previously in Ref. 52, as well as in this study. In the progression from Co_2MnSi (a conventional half metal) to Co_2MnAl (a Weyl semimetal), we hypothesize that Weyl points appear at a composition between $Co_2MnAl_{0.33}Si_{0.67}$ and $Co_2MnAl_{0.67}Si_{0.33}$, resulting in the significant increase of α_{xy}^{A} at $Co_2MnAl_{0.67}Si_{0.33}$. It will be of great interest to investigate the compositions in-between Al-0.33 and Al-0.67.

Our ANC results suggest the existence of Weyl points in $Co_2MnAl_{0.67}Si_{0.33}$ that are too far from the Fermi level to show up in the AHC. The fact that α_{xy}^{A} is sensitive to Weyl points far from the Fermi level reflects the fact that the Nernst effect is proportional to derivatives of the Hall conductivity with respect to energy. As noted by Noky *et al.* [22], although the anomalous Hall conductivity is essentially the integral of the Berry curvature over all states below the Fermi level, α_{xy}^{A} reflects the occupancy of partially-filled states and therefore depends on the derivative of the Fermi distribution function, which decays only algebraically with energy for energy scales on the order of several k_BT. At room temperature, states a few hundred meV above the Fermi level will therefore still contribute to the Nernst effect, even if they do not impact the anomalous Hall conductivity. This is why the $Co_2MnAl_{0.67}Si_{0.33}$ sample shows a very small AHC but a significant ANC. In principle, it is even possible for the ANC to reverse sign, although we believe that the apparent difference in sign between our work and the result on bulk Co_2MnAl reported in Ref. 41 is due to a difference in sign conventions. (Our sign convention is illustrated in Fig. D1 in Appendix D.) The difference

in magnitudes could be due to small shift of the Fermi energy. Opposite signs for α_{xy}^{A} have been reported for Co_2MnGa even with (apparently) the same sign convention (see Sakai *et al.* [15] and Guin *et al.* [50]). These values are included in Fig. 11. A sign change would be expected as the Fermi level is tuned through a Weyl point, and so could occur from sample to sample if the Fermi level shifts due to a slight change in stoichiometry.

VII. CONCLUSION

In conclusion, we report experimental measurements of magnetothermoelectric coefficients in epitaxial $Co_2MnAl_xSi_{1-x}$ and Co_2FeAl Heusler thin films. Our primary result is the observation of a dramatic enhancement of the ANE in $Co_2MnAl_xSi_{1-x}$ with increasing Al composition x, which we believe is due to the appearance of Weyl points in the band sructure as the Al fraction is increased. The technique presented here would be applicable to a wide range of Heusler alloy thin films grown on insulating or semiconductor substrates. The measurement of the magnetothermoelectric coefficients, α_{xy}^{A} in particular, is complementary to traditional electrical transport measurements used in spintronics (such as the AHE) in that they are particularly sensitive to details of the electronic structure, such as the position of the Fermi level and the Berry curvature near critical points. As such, we expect thermoelectric coefficient measurements to be a valuable tool in the characterization of a wide variety of materials for spintronic applications. Finally, there has been much recent interest in spin pumping or spin torque measurements in Heusler/heavy metal heterostructures. In such experiments, more exotic effects such as the longitudinal spin-Seebeck effect (LSSE) [53] or the inverse spin-Hall effect due to spin pumping (ISHE) [54, 55] can give signals that follow the same phenomenology as the ANE. If the film ANC was known *a priori*, the degree to which ANE signals contribute to (or contaminate) the claimed LSSE or ISHE signals could be quantified, providing further motivation for measurement of ANCs.

Several avenues exist to utilize this technique for future study. First, elemental ratios in quaternary full Heusler alloys such as $Co_2Fe_xMn_{1-x}Si$ or $Co_2Fe(Ga_xGe_{1-x})$ have been varied to optimize damping [56] and spin injection properties [57–59]. One could perform ANE measurements on these samples as a characterization tool to help with the optimization process, due to their sensitivity to energy derivatives of the DOS and the Fermi level. Next, the experimentally measured Nernst and Seebeck coefficients for different stoichiometries,

as demonstrated here for $Co_2MnAl_xSi_{1-x}$, can in principle be used to monitor the formation of features such as Weyl points in the band structure.

VIII. ACKNOWLEDGEMENTS

This work was supported by the National Science Foundation under DMR 1708287. The MBE sample growth was performed at University of California, Santa Barbara (UCSB) and was supported by U.S. Department of Energy (contract no. DE-SC0014388). Devices of this work were fabricated in the Minnesota Nano Center, which is supported by the National Science Foundation through the National Nano Coordinated Infrastructure Network (NNCI) under Award Number ECCS-2025124. Sample characterizations were performed in the Characterization Facility, University of Minnesota, which receives partial support from NSF through the MRSEC program under award number EECS-2025124. We thank Professor E. Dan Dahlberg for advice about the collection of the AMR data.

Appendix A: Temperature profile measurement

Determining the Seebeck and anomalous Nernst coefficients requires knowledge of the spatial temperature profile, and this must be quantified before these coefficients can be determined. The thermistor strip shown in Fig. 5(a) allows for 4-wire resistance measurements of the sections labeled 1-4 using a probe current $I_p = 1$ mA. For calibration, the resistance of each thermistor is measured from 2 to 400 K with zero applied heater power. In this temperature range, the resistance of the gold varies quasi-linearly with temperature except at low temperatures ($T \lesssim 30$ K) where the curve flattens due to residual resistivity. A lock-in amplifier is used to measure the magnitude and phase of the local temperature changes in the thermistor upon application of Joule heating power from the heater elements. A sinusoidal ac excitation current $I(t) = \sqrt{2} I_h \sin(\omega t)$ is driven through the heater elements, resulting in power dissipation $P(t) = I^2(t) R_h$. Through the trigonometric identity $\sin^2(\omega t) = \frac{1}{2}[1 - \cos(2\omega t)]$, the dissipated power takes the form

$$P(t) = I_h^2 R_h [1 - \cos(2\omega t)], \tag{A1}$$

where it is clear that the power dissipated has a component at 2ω. The lock-in therefore monitors thermistor resistance changes at 2ω, ensuring measured changes were due to the

applied heater power. The increase in resistance at 2ω is compared to dR_i/dT to determine the local ac temperature profile $T_i^{2\omega}$ of the i-th thermistor element as

$$T_i^{2\omega} = V_i^{2\omega} \left(I_p \frac{dR_i}{dT} \right)^{-1}, \tag{A2}$$

where $V_i^{2\omega}$ is the second harmonic voltage measured in the i-th thermistor. $V_i^{2\omega}$ includes both in-phase and out-of-phase quadrature components with respect to the heater excitation.

Although in principal $V_i^{2\omega}$ may include Seebeck voltages built up along the Au element, it was verified that $V_i^{2\omega}$ inverted sign upon inverting I_p, implying that these contributions were negligible for the I_p values used. Spatial $T^{2\omega}$ profiles measured based on Eq. A2 on the device in Fig. 5(a) are shown in Fig. 5(b) for several choices of drive frequency, $\omega/2\pi$, which are plotted for thermistors 1-4 as a function of their distance from the heater element. In general, a nontrivial spatial dependence of the magnitude and phase of $T^{2\omega}$ along the thermistor strip was observed, motivating the model fits shown in Fig. 5(b). The spatial model of the ac temperature profile to which the fits correspond will be discussed in the following section.

Appendix B: Temperature profile model

To understand the spatial and temporal temperature profile of the thermoelectric devices (as shown in Fig. 5), an analytic time-dependent model of heat diffusion in the device was derived. The device is three-dimensional, and modeling the temperature profile would require solving the heat equation

$$\frac{\partial T}{\partial t} - D\nabla^2 T = f(\mathbf{r}, t), \tag{B1}$$

where D is the thermal diffusivity, T is the temperature, and $f(\mathbf{r}, t)$ is an inhomogeneous source term representing the heaters. However, the geometry of the device allows one to simplify the problem into one dimension along the x direction. First, the temperature gradient is assumed to be perpendicular to the heaters due to the symmetric placement of the Hall bar with respect to the heaters and the aspect ratio of the heaters as compared to the device. Additionally, the heat diffusion into the substrate of the device, $\partial_z T$, is modeled by adding a phenomenological relaxation term, $-rT$, to the one-dimensional heat equation. These simplifying assumptions reduce the homogeneous part of Eq. B1 to the following

one-dimensional differential equation:

$$\frac{\partial T}{\partial t} = D\partial_x^2 T - rT. \tag{B2}$$

One can search for harmonic solutions of the homogeneous part of the heat equation due to the sinusoidal drive current applied to the heaters. We solve Eq. B2 by assuming separation of variables in the form

$$T(x,t) = T(x)e^{i\omega' t}. \tag{B3}$$

Substituting Eq. B3 into Eq. B2,we obtain the following:

$$\partial_x^2 T + k^2 T = 0, k = i(\frac{r + i\omega'}{D})^{1/2}. \tag{B4}$$

This is the well-known Helmholtz equation in one-dimension, which has the solution

$$T(x,t) = A\frac{e^{-k|x|}}{2k}e^{i\omega' t}, \tag{B5}$$

where A is a proportionality constant determined by the heater power and chip/substrate heat capacities. It is worth noting that the prefactor before $e^{i\omega' t}$ in Eq. B5 is in general complex, leading to a spatial dependence of the phase and magnitude of $T(x,t)$, which are both measured by the lock-in X and Y quadratures. The frequency dependence of Eq. 10 is exploited so that thermometry data taken with different heater driving frequencies can be fit simultaneously, which effectively increases the number of points to which the model is fit. The fits to Eq. B5 with A, r, and D as fitting parameters, and $\omega' = 2\omega$ are shown in Fig. 5(b), where it can be seen that the spatial and frequency dependence of the thermistor magnitudes and phases are well-described by Eq. B5. As a check of the success of this model, it is also worth noting that the room temperature thermal diffusivity of MgO derived from this fit is 13 $\mathrm{mm^2 s^{-1}}$, which is within 16 % of the value published in Hofmeister *et al.* [60]. Although several frequencies were used in the fitting in Fig. 5(b), this was mainly to establish the model's validity. Note that because each ΔT_i thermistor recording specified magnitude and phase, effectively 8 (rather than 4) data points are included in a single frequency fit.

Appendix C: Determining the Seebeck coefficient from the $T(x,t)$ profile

The phase-sensitive harmonic lock-in technique detailed in Appendix A is also used to measure Seebeck voltages using pairs of Hall arm leads as shown in Fig. 5(a). If ∇T is not

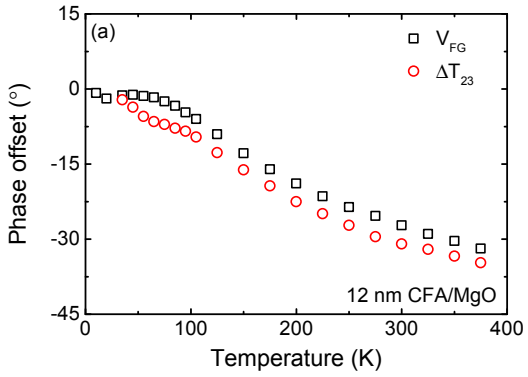

Figure 12: [Color Online] Comparison of the phase offset with respect to heater power for Seebeck voltage (black squares) and thermistor readings (red circles) at an excitation frequency f= 10 Hz. The data shown here are taken on the Co_2FeAl sample.

entirely in the x-direction, additional Seebeck contributions could build up on the Au vias and would be largest on the terminals closest to the heater. To minimize the impact of this effect, the middle pair (V_{FG}) is used to mitigate Seebeck contributions from the Au vias. In any case, the Seebeck coefficient of Au is only a few μV/K over the temperature range studied here [61], which is about a factor of 10 smaller than that of the Heuslers, so any spurious contamination from these Au contributions will only slightly modify the extracted Heusler film Seebeck coefficients.

Because the temperature difference and Seebeck voltage are directly proportional, one would expect that they are in phase with each other. As can be seen in Fig. 12, the second harmonic temperature difference and Seebeck voltages have a nearly identical phase with respect to the heater power over a broad temperature range, lending further credibility to the thermal model. The slight phase discrepancy of about 5° is most likely due to the vertical spatial separation of the thermistors from the contact points where the Seebeck voltage is measured. In principle the complex T from the model and the phase offset could result in a complex Seebeck coefficient, however in practice the Seebeck coefficient should be purely real for driving frequencies far below internal thermal relaxation times. Since the error in phase is slight, the Seebeck coefficient is calculated as,

$$S_{xx} = -\operatorname{sign}(V_{FG}^{2\omega})\frac{|V_{FG}^{2\omega}|}{|T_F^{2\omega} - T_G^{2\omega}|}, \tag{C1}$$

where the vertical bars represent the quadrature amplitude of $V_{FG}^{2\omega}$ and the modulus of complex T, ensuring that the resultant Seebeck coefficient is strictly real. This is then used

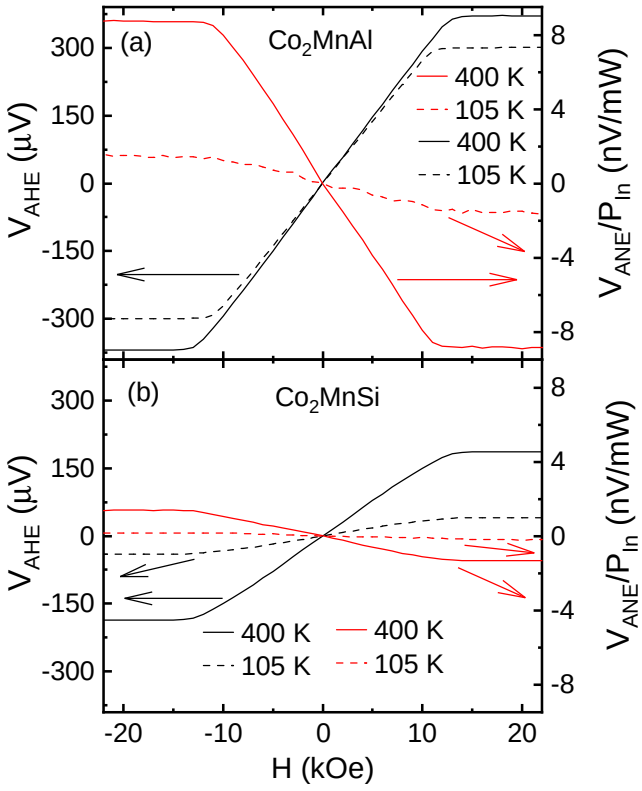

Figure 13: [Color Online] Hall and Nernst (in-phase 2ω component with $f = 10$ Hz heater drive) voltage field sweeps for Co_2MnAl (a) and Co_2MnSi (b) samples taken at temperatures of 105 and 400 K. The heater power used for the Nernst field sweeps for the Co_2MnSi sample was 310 mW at 400 K and 160 mW at 105 K; the heater power used for the Co_2MnAl sample was 450 mW at 400 K and 230 mW at 105 K. The data shown in this figure include subtraction of the ordinary Nernst contribution.

to determine α_{xx} through the relation $\alpha_{xx} = S_{xx}\sigma_{xx}$, which holds if $\rho_{xx} \gg \rho^A_{xy}$.

Appendix D: Determining the Nernst coefficient from the $T(x,t)$ profile

By rewriting Eq. 5 with the definition $S^A_{xy} = E_y/\nabla T$, the anomalous Nernst coefficient, α^A_{xy}, is derived as

$$\alpha^A_{xy} = \frac{\partial_y V}{\partial_x T}\sigma - \frac{\rho^A_{xy}}{\rho_{xx}}\alpha_{xx}, \tag{D1}$$

where the anomalous contribution is the value of α_{xy} with the magnetization saturated along the out-of-plane z-axis after the ordinary Nernst contribution is subtracted. In the Hall bar geometry shown in Fig. 5(a), with the left heater on and the voltage measured across Hall bar contacts A and E, the α_{xy}^{A} may be determined by the relation

$$\alpha_{xy}^{A} = \frac{-V_{EA}^{2\omega}}{l\partial_x T^{2\omega}}\sigma - \frac{\rho_{xy}^{A}}{\rho_{xx}}\alpha_{xx}, \tag{D2}$$

where l is the width of the Hall bar. As in the Seebeck measurement, $V_{EA}^{2\omega}$ is measured using the second harmonic lock-in technique detailed in Appendix A. The form of $T(x,t)$ is known (Eq. B5), and the temperature gradient $\partial_x T^{2\omega}$ can be determined by taking the spatial derivative

$$\partial_x T^{2\omega}(x,t) = -\frac{A}{2}\exp(-(\frac{r+i2\omega}{D})^{1/2}|x|)e^{i2\omega t}, \tag{D3}$$

which allows $\partial_x T^{2\omega}$ to be found for use in Eq. D2 so α_{xy}^{A} can be determined. Unlike ΔT in the Seebeck calculation, the out-of-phase (imaginary) component of $\partial_x T^{2\omega}$ approaches zero for small separations from the heat source [this can be seen graphically in Fig. 5(b)]. Because the pair closest to the heater is used for Nernst voltage, the out-of-phase Nernst voltage is nearly zero and often too small so measure. For this reason, only the real parts of $V_{EA}^{2\omega}$ and $\partial_x T^{2\omega}$ are used to determine α_{xy}^{A}, unlike the phase-dependent Seebeck analysis in which the quadrature amplitude and modulus were taken. In order to distinguish the ANE voltage from the ordinary Nernst effect and background Seebeck contributions, the magnetic field H_z is swept in the out-of-plane orientation, and the Nernst voltage $V_{EA}^{2\omega}$ is recorded. Sample ANE field sweeps are shown in Fig. 13, alongside corresponding AHE sweeps. It should be noted that although a high-field linear slope can be measured in the Nernst geometry, *ordinary* Nernst contributions on the Au vias cannot be reliably subtracted due to the geometry of the Au vias that connect to the Hall bar. Unlike ANE voltages, which only build up along the ferromagnetic Heusler, ONE voltages also build up along the Au vias. These contributions, however, are easily removed by determining the slope of the response at high field.

Due to the fact that there is no universal convention for the definition of positive/negative ANE terminals, we show our convention in Fig. 14.

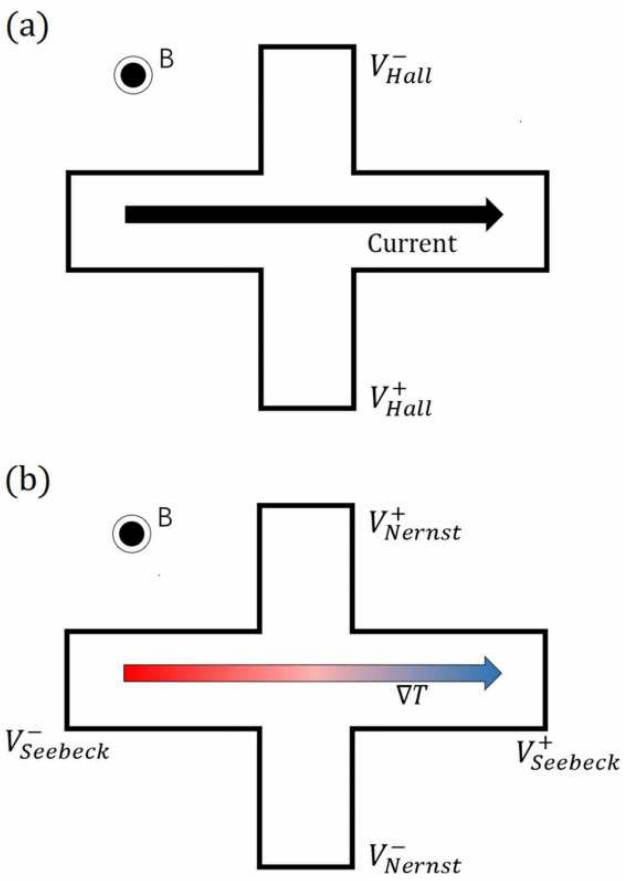

Figure 14: Illustrations of the sign conventions used in this study. (a) Anomalous Hall convention, which follows the ordinary Hall convention. (b) Anomalous Nernst convention. The sign of ANE voltages are reversed from the Hall voltages because the Seebeck voltage is defined in the direction of $-\nabla T$.

---

[1] L. Wollmann, A. K. Nayak, S. S. Parkin, and C. Felser, Heusler 4.0: Tunable materials, Annu. Rev. of Mater. Res **47**, 247 (2017).

[2] R. A. de Groot, F. M. Mueller, P. G. vanEngen, and K. H. J. Buschow, New class of materials: Half-metallic ferromagnets, Phys. Rev. Lett. **50**, 2024 (1983).

[3] D. Comtesse, B. Geisler, P. Entel, P. Kratzer, and L. Szunyogh, First-principles study of spin-dependent thermoelectric properties of half-metallic Heusler thin films between platinum leads, Phys. Rev. B **89**, 094410 (2014).

[4] W. R. Branford, L. J. Singh, Z. H. Barber, A. Kohn, A. K. Petford-Long, W. V. Roy, F. Mag-

nus, K. Morrison, S. K. Clowes, Y. V. Bugoslavsky, and L. F. Cohen, Temperature insensitivity of the spin-polarization in Co_2MnSi films on GaAs (001), New J. Phys **9**, 42 (2007).

[5] M. Jourdan, J. Minr, and J. Braun, Direct observation of half-metallicity in the Heusler compound Co_2MnSi, Nat. Commun **5**, 3974 (2014).

[6] K. Inomata, N. Ikeda, N. Tezuka, R. Goto, S. Sugimoto, M. Wojcik, and E. Jedryka, Highly spin-polarized materials and devices for spintronics, Sci. Technol. Adv. Mater **9**, 014101 (2008).

[7] M. Oogane, Y. Sakuraba, J. Nakata, H. Kubota, Y. Ando, A. Sakuma, and T. Miyazaki, Large tunnel magnetoresistance in magnetic tunnel junctions using Co_2MnX (X = Al, Si) Heusler alloys, Journal of Physics D: Applied Physics **39**, 834 (2006).

[8] C. Guillemard, W. Zhang, G. Malinowski, C. de Melo, J. Gorchon, S. Petit-Watelot, J. Ghanbaja, S. Mangin, P. Le Fvre, F. Bertran, and S. Andrieu, Engineering $Co_2MnAl_xSi_{1-x}$ Heusler Compounds as a Model System to Correlate Spin Polarization, Intrinsic Gilbert Damping, and Ultrafast Demagnetization, Adv. Mater **32**, 1908357 (2020).

[9] C. Liu, C. K. A. Mewes, M. Chshiev, T. Mewes, and W. H. Butler, Origin of low Gilbert damping in half metals, Appl. Phys. Lett **95**, 022509 (2009).

[10] N. Nagaosa, J. Sinova, S. Onoda, A. H. MacDonald, and N. P. Ong, Anomalous Hall effect, Rev. Mod. Phys **82**, 1539 (2010).

[11] Y. Yao, L. Kleinman, A. H. MacDonald, J. Sinova, T. Jungwirth, D. S. Wang, E. Wang, and Q. Niu, First Principles Calculation of Anomalous Hall Conductivity in Ferromagnetic bcc Fe, Phys. Rev. Lett **92**, 037204 (2004).

[12] L. Berger, Side-Jump Mechanism for the Hall Effect of Ferromagnets, Phys. Rev. B **2**, 4559 (1970).

[13] J. Smit, The spontaneous Hall effect in ferromagnetics I, Physica **21**, 877 (1955).

[14] D. Xiao, Y. Yao, Z. Fang, and Q. Niu, Berry-phase effect in anomalous thermoelectric transport, Phys. Rev. Lett **97**, 026603 (2006).

[15] A. Sakai, Y. P. Mizuta, A. A. Nugroho, R. Sihombing, T. Koretsune, M. Suzuki, N. Takemori, R. Ishii, D. Nishio-Hamane, R. Arita, P. Goswami, and S. Nakatsuji, Giant anomalous Nernst effect and quantum-critical scaling in a ferromagnetic semimetal, Nat. Phys **14**, 1119 (2018).

[16] Y. Sakuraba, K. Hasegawa, M. Mizuguchi, T. Kubota, S. Mizukami, T. Miyazaki, and K. Takanashi, Anomalous Nernst Effect in $L1_0$-FePt/MnGa Thermopiles for New Thermoelectric Applications, Appl. Phys. Express **6**, 033003 (2013).

[17] M. Mizuguchi and S. Nakatsuji, Energy-harvesting materials based on the anomalous Nernst effect, Sci. Technol. Adv. Mat **20**, 262 (2019).

[18] J. Ma, V. I. Hegde, K. Munira, Y. Xie, S. Keshavarz, D. T. Mildebrath, C. Wolverton, A. W. Ghosh, and W. H. Butler, Computational investigation of half-Heusler compounds for spintronics applications, Phys. Rev. B **95**, 024411 (2017).

[19] Y. Sakuraba, K. Takanashi, Y. Kota, T. Kubota, M. Oogane, A. Sakuma, and Y. Ando, Evidence of Fermi level control in a half-metallic Heusler compound Co_2MnSi by Al-doping: Comparison of measurements with first-principles calculations, Phys. Rev. B **81**, 144422 (2010).

[20] N. F. Mott and H. Jones, *The Theory of the Properties of Metals and Alloys* (Clarendon Press, Oxford, 1936).

[21] S. Saha and S. Tewari, Anomalous Nernst effect in type-II Weyl semimetals, Eur. Phys. J. B **91**, 1 (2017).

[22] J. Noky, J. Gooth, C. Felser, and Y. Sun, Characterization of topological band structures away from the Fermi level by the anomalous Nernst effect, Phys. Rev. B **98**, 241106(R) (2018).

[23] I. Galanakis, P. Mavropoulos, and P. H. Dederichs, Electronic structure and SlaterPauling behaviour in half-metallic Heusler alloys calculated from first principles, J. Phys. D **39**, 765 (2006).

[24] M. Oogane, A. P. McFadden, Y. Kota, T. L. Brown-Heft, M. Tsunoda, Y. Ando, and C. J. Palmstrøm, Fourfold symmetric anisotropic magnetoresistance in half-metallic Co_2MnSi Heusler alloy thin films, Jpn. J. Appl. Phys **57**, 063001 (2018).

[25] T. L. Brown-Heft, J. A. Logan, A. P. McFadden, C. Guillemard, P. Le Fèvre, F. m. c. Bertran, S. Andrieu, and C. J. Palmstrøm, Epitaxial Heusler superlattice Co_2MnAl / Fe_2MnAl with perpendicular magnetic anisotropy and termination-dependent half-metallicity, Phys. Rev. Materials **2**, 034402 (2018).

[26] P. Webster, Magnetic and chemical order in Heusler alloys containing cobalt and manganese, J. Phys. Chem. Solids **32**, 1221 (1971).

[27] Y. Takamura, R. Nakane, and S. Sugahara, Analysis of l21-ordering in full-heusler co2fesi alloy thin films formed by rapid thermal annealing, J. Appl. Phys **105**, 07B109 (2009).

[28] W. K. Peria, T. A. Peterson, A. P. McFadden, T. Qu, C. Liu, C. J. Palmstrøm, and P. A. Crowell, Interplay of large two-magnon ferromagnetic resonance linewidths and low Gilbert damping in Heusler thin films, Phys. Rev. B **101**, 134430 (2020).

[29] R. Y. Umetsu, K. Kobayashi, A. Fujita, R. Kainuma, and K. Ishida, Phase stability and magnetic properties of $L2_1$ phase in $Co_2Mn(Al_{1x}Si_x)$ Heusler alloys, Scripta. Mater **58**, 723 (2008).

[30] Y. Sakuraba, S. Kokado, Y. Hirayama, T. Furubayashi, H. Sukegawa, S. Li, Y. K. Takahashi, and K. Hono, Quantitative analysis of anisotropic magnetoresistance in Co_2MnZ and Co_2FeZ epitaxial thin films: A facile way to investigate spin-polarization in half-metallic Heusler compounds, Appl. Phys. Lett **104**, 172407 (2014).

[31] Y. Sakuraba, M. Hattori, M. Oogane, Y. Ando, H. Kato, A. Sakuma, T. Miyazaki, and H. Kubota, Giant tunneling magnetoresistance in $Co_2MnSiAlOCo_2MnSi$ magnetic tunnel junctions, Appl. Phys. Lett **88**, 192508 (2006).

[32] H. Liu, Y. Honda, T. Taira, K. Matsuda, M. Arita, T. Uemura, and M. Yamamoto, Giant tunneling magnetoresistance in epitaxial $Co_2MnSi/MgO/Co_2MnSi$ magnetic tunnel junctions by half-metallicity of Co_2MnSi and coherent tunneling, Appl. Phys. Lett **101**, 132418 (2012).

[33] J. Kübler and C. Felser, Berry curvature and the anomalous Hall effect in Heusler compounds, Phys. Rev. B **85**, 012405 (2012).

[34] J. Tung and G. Guo, High spin polarization of the anomalous Hall current in Co-based Heusler compounds, New J. Phys **15**, 033014 (2013).

[35] J. G. Checkelsky and N. P. Ong, Thermopower and Nernst effect in graphene in a magnetic field, Phys. Rev. B **80**, 081413(R) (2009).

[36] J. P. Small, K. M. Perez, and P. Kim, Modulation of thermoelectric power of individual carbon nanotubes, Phys. Rev. Lett **91**, 256801 (2003).

[37] K. Hayashi, M. Eguchi, and Y. Miyazaki, Structural and Thermoelectric Properties of Ternary Full-Heusler Alloys, J. Electron. Mater **46**, 2710 (2017).

[38] B. Balke, S. Ouardi, T. Graf, J. Barth, C. G. Blum, G. H. Fecher, A. Shkabko, A. Weidenkaff, and C. Felser, Seebeck coefficients of half-metallic ferromagnets, Solid State Commun **150**, 529 (2010).

[39] F. J. Blatt, D. J. Flood, V. Rowe, P. A. Schroeder, and J. E. Cox, Magnon-Drag Thermopower in Iron, Phys. Rev. Lett **18**, 395 (1967).

[40] F. J. Blatt, P. A. Schroeder, C. L. Foiles, and D. Greig, *Thermoelectric Power of Metals* (Plenum Press, New York, London, 1976).

[41] Y. Sakuraba, K. Hyodo, A. Sakuma, and S. Mitani, Giant anomalous Nernst effect in the

$Co_2MnAl_{1-x}Si_x$ Heusler alloy induced by Fermi level tuning and atomic ordering, Phys. Rev. B **101**, 134407 (2020).

[42] X. Jia, W. Yang, M. Qin, and L. Wang, Electronic structure and magnetism of the Heusler alloy $Co_2MnSi_{1-x}Al_x$, J. Phys. D **41**, 085004 (2008).

[43] R. Ramos, M. H. Aguirre, A. Anadón, J. Blasco, I. Lucas, K. Uchida, P. A. Algarabel, L. Morellón, E. Saitoh, and M. R. Ibarra, Anomalous Nernst effect of Fe_3O_4 single crystal, Phys. Rev. B **90**, 054422 (2014).

[44] N. Hanasaki, K. Sano, Y. Onose, T. Ohtsuka, S. Iguchi, I. Kézsmárki, S. Miyasaka, S. Onoda, N. Nagaosa, and Y. Tokura, Anomalous Nernst effects in pyrochlore molybdates with spin chirality, Phys. Rev. Lett **100**, 106601 (2008).

[45] Y. Pu, D. Chiba, F. Matsukura, H. Ohno, and J. Shi, Mott relation for anomalous Hall and Nernst effects in $Ga_{1-x}Mn_xAs$ ferromagnetic semiconductors, Phys. Rev. Lett **101**, 117208 (2008).

[46] T. Miyasato, N. Abe, T. Fujii, a. Asamitsu, S. Onoda, Y. Onose, N. Nagaosa, and Y. Tokura, Crossover behavior of the anomalous hall effect and anomalous nernst effect in itinerant ferromagnets, Phys. Rev. Lett **99**, 086602 (2007).

[47] M. Ikhlas, T. Tomita, T. Koretsune, M. T. Suzuki, D. Nishio-Hamane, R. Arita, Y. Otani, and S. Nakatsuji, Large anomalous Nernst effect at room temperature in a chiral antiferromagnet, Nat. Phys **13**, 1085 (2017).

[48] X. Li, L. Xu, L. Ding, J. Wang, M. Shen, X. Lu, Z. Zhu, and K. Behnia, Anomalous Nernst and Righi-Leduc Effects in Mn_3Sn: Berry Curvature and Entropy Flow, Phys. Rev. Lett **119**, 056601 (2017).

[49] Y. Hirokane, Y. Tomioka, Y. Imai, A. Maeda, and Y. Onose, Longitudinal and transverse thermoelectric transport in MnSi, Phys. Rev. B **93**, 014436 (2016).

[50] S. N. Guin, K. Manna, J. Noky, S. J. Watzman, C. Fu, N. Kumar, W. Schnelle, C. Shekhar, Y. Sun, J. Gooth, and C. Felser, Anomalous Nernst effect beyond the magnetization scaling relation in the ferromagnetic Heusler compound Co_2MnGa, NPG. Asia. Mater **11**, 16 (2019).

[51] J. Kbler and C. Felser, Weyl points in the ferromagnetic Heusler compound Co_2MnAl, Europhys. Lett. **114**, 47005 (2016).

[52] P. Li, J. Koo, W. Ning, J. Li, L. Miao, L. Min, Y. Zhu, Y. Wang, N. Alem, C. Liu, Z. Mao, and B. Yan, Giant room temperature anomalous Hall effect and tunable topology in a ferro-

magnetic topological semimetal Co_2MnAl, Nat. Commun. **11**, 3476 (2020).

[53] G. E. Bauer, E. Saitoh, and B. J. Van Wees, Spin caloritronics, Nat. Mater **11**, 391 (2012).

[54] Y. Tserkovnyak, A. Brataas, and G. E. W. Bauer, Enhanced Gilbert Damping in Thin Ferromagnetic Films, Phys. Rev. Lett **88**, 117601 (2002).

[55] E. Saitoh, M. Ueda, H. Miyajima, and G. Tatara, Conversion of spin current into charge current at room temperature: Inverse spin-Hall effect, Appl. Phys. Lett **88**, 182509 (2006).

[56] B. S. D. C. S. Varaprasad, A. Srinivasan, Y. K. Takahashi, M. Hayashi, A. Rajanikanth, and K. Hono, Spin polarization and Gilbert damping of $Co_2Fe(Ga_xGe_{1-x})$ Heusler alloys, Acta. Mater **60**, 6257 (2012).

[57] T. Kubota, S. Tsunegi, M. Oogane, S. Mizukami, T. Miyazaki, H. Naganuma, and Y. Ando, Half-metallicity and Gilbert damping constant in $Co_2Fe_xMn_{1-x}Si$ Heusler alloys depending on the film composition, Appl. Phys. Lett **94**, 122504 (2009).

[58] T. A. Peterson, S. J. Patel, C. C. Geppert, K. D. Christie, a. Rath, D. Pennachio, M. E. Flatté, P. M. Voyles, C. J. Palmstrøm, and P. A. Crowell, Spin injection and detection up to room temperature in Heusler alloy/ n-GaAs spin valves, Phys. Rev. B **94**, 235309 (2016).

[59] K. D. Christie, Non-equilibrium spin accumulation in $Co_2Fe_xMn_{1-x}Si$/n-GaAs heterostructures, Ph.D. thesis, University of Minnesota (2014).

[60] A. M. Hofmeister, Thermal diffusivity and thermal conductivity of single-crystal MgO and Al_2O_3 and related compounds as a function of temperature, Phys. Chem. Minerals **41**, 361 (2014).

[61] N. Cusack and P. Kendall, The Absolute Scale of Thermoelectric Power at High Temperature, Proc. Phys. Soc **72**, 898 (1958).